# Revealing the Mechanism of Sodium Diffusion in $Na_xFePO_4$ Using an Improved Force Field

Mauricio R. Bonilla,[*,†] Ariel Lozano,[†] Bruno Escribano,[†] Javier Carrasco,[‡] and Elena Akhmatskaya[†,¶]

†*Basque Center for Applied Mathematics, Alameda de Mazarredo 14 (48009) Bilbao, Spain*

‡*CIC EnergiGUNE, Albert Einstein 48 (01510) Miñano, Spain*

¶*IKERBASQUE, Basque Foundation for Science (48013) Bilbao, Spain*

E-mail: mrincon@bcamath.org

## Abstract

Olivine $NaFePO_4$ is a promising cathode material for Na-ion batteries. Intermediate phases such as $Na_{0.66}FePO_4$ govern phase stability during intercalation-deintercalation processes, yet little is known about $Na^+$ diffusion in $Na_xFePO_4$ ($0 < x < 1$). Here we use an advanced simulation technique, Randomized Shell Mass Generalized Shadow Hybrid Monte Carlo Method (RSM-GSHMC) in combination with a specifically developed force field for describing $Na_xFePO_4$ over the whole range of sodium compositions, to thoroughly examine $Na^+$ diffusion in this material. We reveal a novel mechanism through which $Na^+/Fe^{2+}$ antisite defect formation halts transport of $Na^+$ in the main diffusion direction [010], while simultaneously activating diffusion in the [001] channels. A similar mechanism was reported for $Li^+$ in $LiFePO_4$, suggesting that a transition from one- to two-dimensional diffusion prompted by antisite defect formation is common to olivine structures, in general.

1

# Introduction

Today's commercial rechargeable batteries rely on Li-ion technology. Yet the expansion of the battery market toward electric vehicles and large-scale grid storage creates some important concerns.[1] One particular worry is that a massive use of lithium in the future will probably be tied to steeply increasing prices and sustainability issues. Thus convenient alternatives to lithium are needed. From a chemical viewpoint, sodium is positioned immediately below lithium in the periodic table and, therefore, it is its natural surrogate.[2,3] Added to this, the high abundance, environment-friendly nature, and low cost of sodium have made research in Na-based batteries a topic of high interest in recent years.[4–12]

For the past few decades, research in Li-ion batteries has been racing to gather knowledge on the redox chemistry between lithium and a wide range of host materials (see, e.g. Nitta et al.[13] for a brief review). Despite the chemical similarity between lithium and sodium, these accomplishments must be taken with caution when considering analogous Na-based electroactive materials. One prominent example is graphite, which is commonly used as anode in today's Li-ion batteries;[14,15] yet graphite does not intercalate sodium under moderate conditions.[16,17] The origin of this difference has remained a mistery for a long time. Only very recently, first-principles calculations were able to shed light into this issue by showing that Li–C bonds in graphite are enhanced due to a covalent contribution, which is missing in the case of Na–C bonds and makes Na-intercalated graphite unstable.[18] This particular example highlights two important general conclusions: (*i*) beyond obvious differences of mass and size between lithium and sodium cations, the chemical behavior (i.e. electrochemial performance) of Li- and Na-intercalated compounds can also be very different due to electronic structure effects; and (*ii*) atomistic modeling is a useful approach to close the existing gap between our extensive knowledge on Li-based electroactive materials and equivalent Na-based ones.

Here we use atomistic modeling to examine a promising cathode material for Na-ion batteries, olivine $NaFePO_4$. From a Li-based viewpoint, sustainability, and cost driven

research on polyanionic iron-based materials has led us to olivine $LiFePO_4$, which has clearly been the most studied one to date among commercial cathode materials.[19] $LiFePO_4$ shows stand-out features such as high stability, high rate capability, and sustained high voltage throughout the whole discharge cycle. In principle, one could expect $NaFePO_4$ to inherit these properties from its isostructural lithium counterpart. Therefore, there has been a recent flurry of interest in $NaFePO_4$ (see, e.g. Fang et al.[20]). The first fundamental studies revealed that the intercalation chemistry of lithium and sodium in $FePO_4$ are, however, significantly different.[21,22] These differences are generally attributed to the formation of ordered partially sodiated structures in the case of $NaFePO_4$[20,23–25] as opposed to the single-phase behavior of $LiFePO_4$.[26–28] The formation of stable $Na^+$ arrangements adds therefore structural complexity to the study of sodium intercalation at the molecular level. This issue is particularly relevant when studying dynamic properties such as $Na^+$ mobility using simulations, requiring large supercells and long simulation times to account for possible sodium orderings. These requirements make the use of first-principles methods, such as density funtional theory (DFT), prohibitive in terms of computational cost.

Our study addresses this computational challenge as follows. First, we have chosen to apply an enhanced sampling technique instead of conventional molecular dynamics (MD) in order to mitigate the need for too long simulation times. In particular, we have used the Randomized Shell Mass Generalized Shadow Hybrid Monte Carlo method (RSM-GSHMC), which we developed and tested on olivine $NaFePO_4$ before.[29] Second, we have developed a robust force field for $NaFePO_4$ in order to effectively reduce the computational cost associated with DFT calculations when dealing with large supercells, without sacrificing accuracy and predictiveness. The proposed new force field includes polarizability effects through a core–shell model and it has specifically been designed to describe simultaneously $Fe^{2+}$ and $Fe^{3+}$. This is important because partially sodiated $FePO_4$ (which we will refer to as $Na_xFePO_4$) contains a mixture of $Fe^{2+}$ and $Fe^{3+}$ species due to the presence of $Na^+$ vacancies in the structure. In this regard, the proposed force field goes beyond the previously suggested

interatomic potentials for $NaFePO_4$, which were specifically derived to simulate fully sodiated structures and thus are only valid when one type of iron species, $Fe^{2+}$, is present.[30,31] Notably, our force field is parametrized using an extensive DFT-based configuration data set that covers a wide range of sodium concentrations. This aspect provides a level of predictibility not available in force fields obtained from a limited amount of experimental data.

In the following, we first set out the details of the new developed force field for $Na_xFePO_4$. Then we thoroughly discuss accuracy and sampling efficiency aspects of our proposed simulation approach. Finally our main results are reported and analyzed on the basis of calculated $Na^+$ diffusion pathways at different temperatures and sodium concentrations, comparing the performance of conventional MD and RSM-GSHMC simulations combined with the new and previously known force fields. Our findings reveal novel $Na^+$ diffusion dynamics, which actively involves the formation of $Na^+/Fe^{2+}$ antisite defects. Such defect formation processes are generally assumed to take place during ion intercalation in polyanionic iron-based materials,[32,33] but this is the first time that they have directly been visualized in atomistic simulations. Finally, we put forward that the accelerated sampling provided by the RSM-GSHMC method can be a very useful technique to observe, in general, this kind of rare events in solid state ionics within reasonable simulation time scales.

## Development of the New Force Field

Understanding $Na^+$ diffusion in $Na_xFePO_4$ is fundamentally important when considering its use as a cathode material in Na-ion batteries. While DFT studies have provided valuable insights into a range of materials properties,[34,35] these works are limited to short time-scales over prespecified migration paths. In order to explore longer time-scales without migration path constrains, simpler classical interatomic potentials are needed.[36–39] The development of such potentials (i.e., a force field) has three fundamental requirements:

- an appropriate functional form of an interaction potential,

- a training data set of structural, mechanical and/or thermodynamic properties (e.g. experimental, computed, etc.) to fit the model and

- an optimization strategy to perform the fitting.

In the following subsections, these three aspects are described specifically for the development of a new force field for $Na_xFePO_4$.

## Force Field Model

Long-range electrostatic interactions in ionic liquids or metal oxides, including all typical metal-ion cathodes, represent a challenge for the development of accurate force fields. In particular, ionic polarizability in these materials can be strong enough to significantly influence thermodynamic and transport properties.[40–43] In this work, ionic polarizability is described through the core–shell model suggested by Dick and Overhauser,[44] in which a central core of a charge $X$ and a shell of a charge $Y$ are introduced in such a way that the sum of these charges $X + Y$ equals to the valence state of the ion. The core and shell are coupled together in a unit via a harmonic potential, which allows the shell to move with respect to the core, thus simulating a dielectric polarization. Following Whiteside et al.,[31] only the $Fe^{2+}$ and the $O^{2-}$ ions are split into core–shell units. Hereafter, $O_{sh}$ and $Fe_{sh}$ will refer to the $O^{2-}$ and $Fe^{2+}$ shells, respectively.

The total potential energy in our model is given by

$$U_{tot} = U_C + U_{Born} + U_{CS} + U_{angle}, \tag{1}$$

where $U_C$ represents long-range Coulomb interactions, $U_{Born}$ short-range repulsion and long-range van der Waals forces, $U_{CS}$ is the interaction within core–shell units and $U_{angle}$ is an angular term for the $PO_4$ tetrahedral units.

Coloumbic interactions are explicitely given by

$$U_C = \frac{1}{4\pi\epsilon} \sum_{i,j=1}^{N} \frac{q_i q_j}{r_{ij}}, \tag{2}$$

where $\epsilon$ is the vacuum permittivity; $r_{ij}$ is the distance between particles $i$ and $j$; $q_i$ and $q_j$ are their respective charges; and $N$ is the total number of particles. The Born interaction is described by[45]

$$U_{Born} = \sum_{i,j=1}^{N} A_{ij} exp\left(-\frac{r_{ij}}{\rho_{ij}}\right) - \frac{C_{ij}}{r_{ij}^6} + \frac{D_{ij}}{r_{ij}^8}, \tag{3}$$

where, $A_{ij}$, $\rho_{ij}$, $C_{ij}$ and $D_{ij}$ are positive constants defining the shapes of the repulsive and attractive terms of the potential.

The core–shell interaction energy is estimated as

$$U_{CS} = \frac{1}{2} \sum_{l=1}^{L} k_l r_l^2, \tag{4}$$

where $k_l$ is the spring constant for the $l$–th core–shell unit, $r_l$ is the core–shell distance, and $L$ is the total number of shells. Importantly, neither Coloumbic nor Born interactions are computed within core–shell units. Moreover, for ions described as core–shell units only the shells are involved in the estimation of Born interactions, while the cores participate only electrostatically.

Following Whiteside et al.,[31] a three-body angular interacion ($O_{sh}$-P-$O_{sh}$) in the $PO_4$ tetrahedral units is also included

$$U_{angle} = \sum_{k=1}^{K} \frac{1}{2} k_{ang} (\theta_k - \theta_0)^2, \tag{5}$$

where $k_{ang}$ is the spring constant, $\theta_0$ is the equilibrium bond angle, $\theta_k$ is the current value of the bond $k$, and $K$ is the total number of angle interactions.

Two main approaches are found in the literature to simulate core–shell systems: the

so-called shell relaxation (CS-min) scheme[46] and the adiabatic shells (CS-adi) method.[40]

In the CS-min scheme an energy minimization is performed after each MD step in order to update the shell positions, making this approach very computationally demanding. Conversely, in the CS-adi method, a small fraction $y$ of the ion mass is put on the shell, whereas the remaining $1–y$ fraction is left to the core. Then, all the particle positions propagate following the conventional MD technique. For a sufficiently small value of $y$, the shells adiabatically follow the cores motion during the simulation. However, the period of the core–shell spring is proportional to $\sqrt{y(y-1)}$,[40] which means that a small $y$ requires a small integration time-step. In recent work from this group, a systematic methodology was proposed to introduce a shell mass in a way that minimizes the negative effect on the kinetic energy of the system.[29] This methodology is used in the present study.

## Parameter Estimation with *potfit*

The program *potfit*[47,48] was chosen to parametrize the proposed force field. *potfit* makes use of the force - matching method,[49] in which the potential parameters are adjusted to optimally reproduce forces, stresses and energies from reference data obtained through first - principles calculations.

All reference configurations in this study were computed using the plane wave DFT code VASP.[50,51] For configuration $m$ consisting of $N_m$ particles, VASP calculates one energy $e_m^0$, six components of the stress tensor $s_{m,l}^0$, $(l = 1, ..., 6)$ and $3N_m$ Cartesian force components, $f_{m,n}$, $(n = 1, ..., 3N_m)$. The details of the generated DFT database are provided in the next subsection, while the cost function implemented in *potfit*[47,48] is described in section S1 of the Supporting Information (SI).

Instead of allowing all parameters to freely vary, only the van der Waals parameters between oxygen shells ($O_{sh}$–$O_{sh}$) and those from the angular contribution ($O_{sh}$–P–$O_{sh}$) were estimated. All other parameters were left as originally proposed by Whiteside et al.[31] It was not necessary to modify the parameters for other species because the most significant effect

observed when removing $Na^+$ from the $NaFePO_4$ system was an anomalous displacement of the $(PO_4)^{3-}$ units (see section S3 in the SI). Hence, training the Born potential in order to capture the $O_{sh}$–$O_{sh}$ repulsion in the presence of a neighboring vacancy was enough for producing a robust force field applicable to materials with different sodium concentrations.

It is important to properly select the initial location of the shells prior to the minimization procedure. In section S2 of the SI a simple and consistent solution to perform this task is provided. Finally, we must note that the *potfit* package was modified to introduce the Born model, the damped shifted force method for the Coulomb sum and the three-body angular interactions. In addition, we tuned some built-in parameters as described in the S.I. and introduced the option to ignore Coulomb interactions within the core–shell units.

## Development of the DFT Database

We generated a set of 58 olivine $Na_xFePO_4$ configurations consisting of (a) 11 geometrically optimized structures at 0 K, ranging from 72 to 84 atoms (3 unit cells in the [010] direction) and (b) 58 equilibrated snapshots taken out of *ab initio* MD trajectories, from an ideal $NaFePO_4$ crystal at 500 and 1000 K.

To obtain the geometrically optimized structures, spin-polarized DFT calculations were performed as implemented in the VASP code[51,52] at different sodium concentrations: $x = 1.0, 0.83, 0.66, 0.58$ and $0.0$. We used as a reference the published convex hull of $Na_xFePO_4$ at 0 K.[53] As shown by Saracibar et al.,[53] the intermediate phases at $x = 0.83$ and $x = 0.66$ govern phase stability during intercalation/deintercalation. Moreover, for $x > 0.5$ certain structures display negative formation energies and thus are likely to exist in a metastable form for brief periods of time. On the other hand, all structures with $x < 0.5$ are unstable. Many distinct supercells can be built satisfying $x = 0.83$, 0.66 and 0.58. Hence, for every $x$ we chose the three configurations having the lowest formation energies as reported by Saracibar et al.[53]

Projector augmented wave potentials[54] were employed to replace the inner electrons,

whereas Na (3s), Fe (3p, 3d, 4s), P (3s, 3p), and O (2s, 2p) valence electrons were expanded in plane-waves with a cutoff energy of 600 eV. The Perdew–Burke–Ernzerhof (PBE)[54] exchange-correlation functional was used together with a Monkhorst-Pack grid with at least 2×4×5 k-point sampling per 1×1×1 unit cell. In order to describe the localized Fe 3d states a Hubbard U-like term was added to the PBE functional.[55] Here we used a value of U = 4.3 eV for Fe atoms, as proposed by Zhou et al.[56] for LiFePO$_4$. The 11 structures were fully optimized (cell parameters, volume cells, and atomic positions) with a residual force threshold of 0.02 eV/Å. These computational settings guarantee a tight convergence in total energies (less than 5 meV per formula unit).

Starting from the optimal olivine NaFePO$_4$, *ab initio* MD simulations were performed at 500 and 1000 K using VASP.[51,52] The model system was first thermally equilibrated in a microcanonical ensemble (NVE) for 2 ps and then run for 20 ps in a canonical ensemble (NVT) at the chosen temperatures controlled by a Nose Hoover thermostat.[57] 42 configurations at 500 K and 16 configurations at 1000 K were extracted from the production runs and subsequently incorporated into the training data set.

Optimization of the force field parameters with *potfit* completed with the following root mean -square -errors (eq. S1 in the SI): $\Delta F_f = 0.32$ eV/Å, $\Delta F_s = 0.014$ eV/Å$^3$ and $\Delta F_e = 1.49$ eV. The resulting parameters are listed in Table 1. We refer to the force field developed here as Na$_x$FePO$_4$-ff, whereas that from Whiteside et al.[31] as Whiteside-ff. It is interesting to note that the van der Waals parameters for Fe$^{2+}$–Osh$^{2-}$ worked very well to describe the Fe$^{3+}$–Osh$^{2-}$ interaction. It is possible that optimizing the Fe$^{3+}$–O$_{sh}^{2+}$ parameters could lead to some slight improvement, and, indeed, we tried this alternative. However, the fact that the concentrations of Fe$^{3+}$ depends on $x$ makes such optimization particularly complex. In our case, given that more configurations are available at high $x$ in the data set, the parameters for Fe$^{3+}$ obtained through simulated annealing favored richly sodiated configurations. On the other hand, those with low $x$ expanded unrealistically due to excessive Fe$^{3+}$–O$_{sh}^{2-}$ van der Waals repulsion. Focusing only on O$_{sh}^{2-}$–O$_{sh}^{2-}$ and O$_{sh}^{2-}$–P–O$_{sh}^{2-}$ (P and O$_{sh}^{2-}$ concentrations are

independent of $x$) leads to excellent results without the need for a much larger database.

In the coming sections, we proceed to perform atomistic simulations using different techniques, such as MD and RSM-GSHMC, to validate and test the new force field. The validation includes comparison with DFT simulations, other force fields and experimental results when available.

Table 1: Force Field Parameters for Olivine $Na_xFePO_4$ obtained with *potfit* ($Na_xFePO_4$-ff). Only the parameters corresponding to the $O_{sh}$–$O_{sh}$ and $O_{sh}$ - P - $O_{sh}$ differ from those estimated by Whiteside et al., which are reported in parenthesis.

Born-Mayer-Huggins

| Interactions | $A$ (eV) | $\rho$ (Å) | $C$ (eV Å$^6$) | $D$ |
|---|---|---|---|---|
| $Na^+$ - $O_{sh}^{2-}$ | 629.768 | 0.317 | 0.0 | 0.0 |
| $Fe_{sh}^{2+}$- $O_{sh}^{2-}$ | 1105.241 | 0.311 | 0.0 | 0.0 |
| $Fe^{3+}$- $O_{sh}^{2-}$ | 1105.241 | 0.311 | 0.0 | 0.0 |
| $P^{5+}$ - $O_{sh}^{2-}$ | 897.265 | 0.358 | 0.0 | 0.0 |
| $O_{sh}^{2-}$ - $O_{sh}^{2-}$ | 1506.355 | 0.100 | 36.212 | 1.01 |
| | (22764.3) | (0.149) | (44.53) | (0.0) |

Core–shell

| Species | Core charge | Shell charge | $k$ (eV Å$^{-2}$) |
|---|---|---|---|
| $Fe^{2+}$ | -0.997 | 2.997 | 19.26 |
| $O^{2-}$ | 0.96 | -2.96 | 65.0 |

Angular

| Bond | $k_{ang}$ (eV rad$^{-2}$) | $\theta_0$ (deg) |
|---|---|---|
| $O_{sh}^{2-}$-$P^{5+}$-$O_{sh}^{2-}$ | 4.159 | 109.47 |
| | (1.323) | (109.47) |

# Validation

We check accuracy and performance of the newly proposed force field by comparing the computed structural parameters, unit cell volumes and diffusion coefficients against those obtained with Whiteside-ff, DFT and experiments when varying temperature and $Na^+$ concentration.

## Methodology and Simulation Setup

Both force fields presented in Table 1 were implemented in the open source MD software MultiHMC-GROMACS. This is an in-house software package for atomistic simulations based on GROMACS version 4.5.4,[58] which was modified to use hybrid Monte Carlo based methods[59–61] and multistage integration schemes.[62–64] It is available for public use under the GNU Lesser General Public License.

As samplers, we alternatively used standard MD with a velocity Verlet integrator and RSM-Generalized Shadow Hybrid Monte Carlo (RSM-GSHMC)[29] with the two-stage MAIA integrator.[64]

The GSHMC method is a type of hybrid Monte Carlo (HMC) which offers several improvements over standard HMC and MD by using modified energies instead of true Hamiltonians for sampling, in order to increase the sampling efficiency. The modified energies or shadow Hamiltonians are better conserved by symplectic integrators, leading to a faster convergence of GSHMC compared with HMC. The partial momentum update introduced in GSHMC allows for retaining dynamical information, and thus makes the method applicable to simulation of diffusion processes. The GSHMC method is particularly useful when studying multidimensional spaces and rare events. In this study it is chosen to improve the sampling of the ionic diffusivity of $Na_xFePO_4$. The details of the GSHMC method and its implementation can be found elsewhere.[61,65–69]

In RSM-GSHMC, a mass randomization is applied to the masses of the shells $O_{sh}^{2-}$ and $Fe_{sh}^{2+}$. This helps to reduce any potential negative effects on the kinetic properties of the system when using an adiabatic core–shell model. In this study, RSM-GSHMC is combined with the MAIA integrator which provides the highest accuracy among all other two-stage splitting methods including Verlet.

Prior to performing the simulations, all systems were first stabilized using the steepest descent method for energy minimization. This was followed by 50 ps of equilibration at constant temperature and another 50 ps at constant pressure. The Andersen barostat[70] was

used to impose constant pressure for both MD and GSHMC as implemented in MultiHMC-GROMACS.[66] In MD we used a Nose-Hoover thermostat[57] while the GSHMC method keeps constant temperature by design.[61] We used the force field parameters presented in Table 1 with a cutoff of 12 Å for electrostatics. Periodic boundary conditions were applied in the three dimensions. The production simulations for various sodium concentrations between $x = 0$ and $x = 1$ were run in the NPT ensemble over 10 ns at temperatures ranging between 10 and 900 K, at a pressure of 1 bar using a time step of 1 fs. For all the results presented in this section, we employed $4^{th}$ order shadow Hamiltonians and fixed the GSHMC parameters to L=500 steps for trajectory lengths between Monte Carlo steps and to $\phi = 0.1$ for the partial momentum update.

## Accuracy

In order to assess the accuracy of the newly proposed force field, we measure the unit cell parameters for $Na_xFePO_4$ after a 3 ns simulation using RSM-GSHMC at a constant pressure of 1 bar and a temperature of 300 K. Simulations are performed for systems with $Na^+$ concentrations $x = 0$, 0.58, 0.66, 0.83, and 1. In Table 2 the simulation results alongside with the experimental and DFT values[53] are shown. Data for $x = 0.58$ are not included given the lack of experiments and independent DFT values to compare with. Nevertheless, it is worth mentioning that simulations using Whiteside-ff crash at this concentration.

We found that the divergence between the unit cell parameters calculated using two different force fields was small, although $Na_xFePO_4$-ff achieved values slightly closer to the experimental results. It was also found that $Na_xFePO_4$-ff succeeded in simulations of a wider variety of sodium ion concentrations, while simulations using Whiteside-ff became numerically unstable for $x < 0.66$ (see figure S3 in SI). Instability in the Whiteside-ff is not surprising since the parameters were obtained by fitting with respect to the experimental bond lengths and unit cell parameters of fully sodiated $NaFePO_4$. In this regard, there is no expectation for this force field to be applicable at lower levels of sodiation. In particular, the presence of

sodium vacancies are likely to produce instabilities in systems simulated with Whiteside-ff, given that this force field does not account for the presence of $Fe^{3+}$.

Table 2: Computed lattice constants of olivine $Na_xFePO_4$ using RSM-GSHMC for varying concentrations of $Na^+$ at 300 K with both force fields. Experimental and DFT values are taken from Saracibar et al.[53]

|  | Param. (Å) | Exp. | DFT | Whiteside-ff | $Na_xFePO_4$-ff |
|---|---|---|---|---|---|
| $FePO_4$ | a | 9.81 | 9.97 | – | 9.49 |
|  | b | 5.79 | 5.92 | – | 5.78 |
|  | c | 4.78 | 4.87 | – | 4.74 |
| $Na_{0.66}FePO_4$ | a | 10.28 | 10.41 | 10.13 | 10.33 |
|  | b | 6.08 | 6.06 | 6.08 | 6.03 |
|  | c | 4.93 | 4.99 | 5.09 | 5.01 |
| $Na_{0.83}FePO_4$ | a | 10.31 | 10.45 | 10.49 | 10.37 |
|  | b | 6.11 | 6.19 | 6.08 | 6.23 |
|  | c | 4.95 | 4.99 | 5.03 | 4.94 |
| $NaFePO_4$ | a | 10.41 | 10.50 | 10.32 | 10.45 |
|  | b | 6.22 | 6.27 | 6.33 | 6.26 |
|  | c | 4.95 | 4.99 | 5.07 | 4.99 |

In Figure 1 the volume expansion for a unit cell is presented for temperatures from 10 K to 900 K for a fully sodiated $NaFePO_4$ system computed with RSM-GSHMC using both Whiteside-ff and $Na_xFePO_4$-ff. One can see that the two force fields produce similar trends, although the unit cell volume calculated with $Na_xFePO_4$-ff is generally higher and in better agreement with the experimental results taken from Moreau et al.[71] We notice that Whiteside-ff provides a slightly more accurate estimate of $dV/dT$ than does $Na_xFePO_4$-ff, which is of interest for computing the thermal expansion coefficient. However, for the calculation of the diffusivity, we expect $Na_xFePO_4$-ff to perform better, because at this level of confinement, diffusion is extremely sensitive to small changes in the cross section area of the transport channels and the sites volume (see e.g. Krishna and Van Baten[72]). It is also important to mention that Whiteside-ff at temperatures above 700 K could not produce numerically stable simulations as a result of exceedingly large forces between oxygen shells.
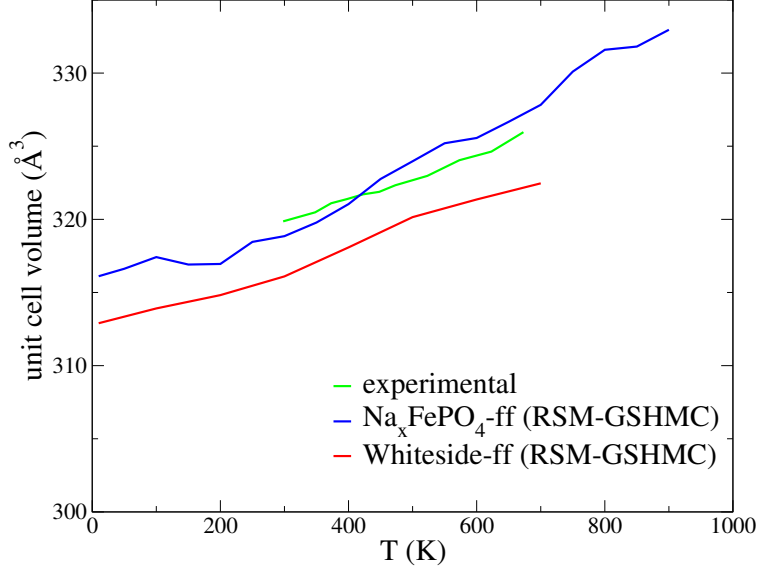
Figure 1: Unit cell volume expansion for temperatures from 10 to 900 K for a fully sodiated NaFePO$_4$ system computed using RSM-GSHMC with Whiteside-ff and Na$_x$FePO$_4$-ff. Experimental results are taken from Moreau at al.[71] For temperatures above 700 K, Whiteside-ff could not produce numerically stable simulations.

## Sampling Efficiency

Once it has been established that Na$_x$FePO$_4$-ff can reproduce structural parameters accurately, we measure its performance by studying the rare events dynamics of Na$^+$ diffusion in Na$_x$FePO$_4$. For the following simulations, we focus on $x = 0.66$, as this ratio between ions and vacancies is a stable intermediate phase and, therefore, interesting for the study of charge transport dynamics during cycling.[53] The diffusion coefficient is a notoriously difficult property to measure in solid state atomistic simulations, requiring exceedingly large systems and very long simulated times. Thus a force field which can more efficiently replicate the rare jumps of Na$^+$ ions along the crystallographic structure combined with an enhanced sampling algorithm would be highly advantageous.

Simulations of 10 ns were performed with temperatures ranging from 10 to 900 K using RSM-GSHMC combined with the two force fields and MD with Na$_x$FePO$_4$-ff. Diffusion at temperatures below 300 K was very difficult to observe, indicating that even longer simulations might be required. However, it was found that the number of ionic jumps is higher
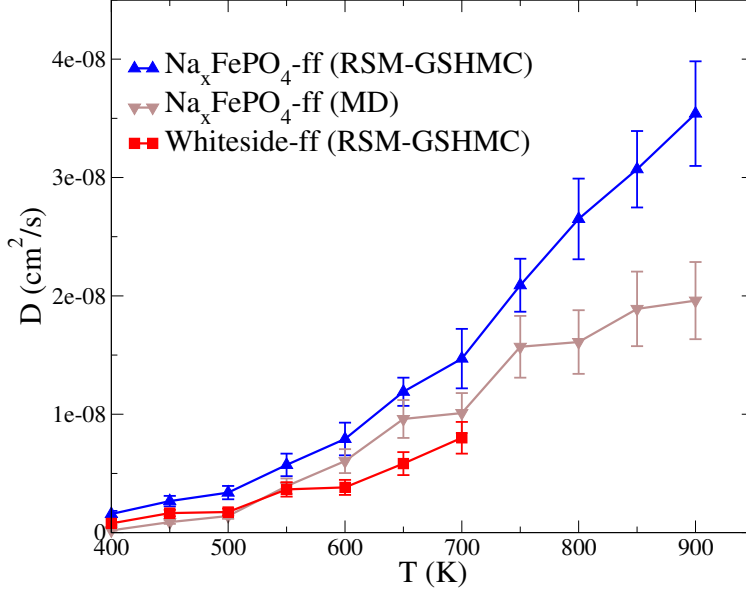
Figure 2: Three-dimensional diffusion coefficient and corresponding error bars at temperatures between 400 and 900 K for a $Na_{0.66}FePO_4$ system using both Whiteside-ff and $Na_xFePO_4$-ff. The divergence observed at high temperatures is a consequence of the improved sampling efficiency of the chosen sampler. At temperatures above 700 K, Whiteside-ff could not produce numerically stable simulations.

when using $Na_xFePO_4$-ff instead of Whisteside-ff at temperatures above 0 K. For instance, at 600 K, each $Na^+$ performs in average $\sim 4$ jumps/ns using $Na_xFePO_4$-ff, while only $\sim 2$ jumps/ns using Whiteside-ff. $Na_xFePO_4$-ff does not lead to numerical instabilities, although at temperatures above 900 K the system becomes amorphous. This is in agreement with experimental observations using X-ray diffraction.[71]

The diffusion coefficients are estimated from the mean square displacements (MSD) according to[58]

$$D = \lim_{t \to \infty} \frac{1}{2nt} \langle \|\vec{r}_i(t) - \vec{r}_i(0)\|^2 \rangle_{i \in \{Na^+\}}, \tag{6}$$

where $n$ is dimensionality (1, 2 or 3 for one, two or three-dimensional diffusion, respectively), $\vec{r}_i$ is the position of atom $i$ and $\{Na^+\}$ is the set of sodium atoms in the simulation box.

Figure 2 shows the three-dimensional diffusion coefficients of $Na^+$ for a range of tempera-

15

tures using RSM-GSHMC with both force fields. We also plot results for similar simulations using standard MD with $Na_xFePO_4$-ff. Comparison of the three curves suggests that not only does the force field affects the diffusion coefficients but the sampling efficiency of the chosen sampler also does. Indeed, at higher temperatures the computed diffusions using MD and RSM-GSHMC combined with the same force field (for equal simulation times) diverge visibly. This is a consequence of the higher sampling efficiency of GSHMC methods.[61] For longer simulation times, both methods are expected to converge.[29]

This is also confirmed by Figure 3, which presents the MSD for $Na^+$ at 700 K in the main diffusion direction, [010], obtained from both traditional MD and RSM-GSHMC. Convergence to the equilibrium slope that provides the diffusion coefficient is reached nearly 2 ns quicker through RSM-GSHMC, demonstrating its ability to sample the configurational space more efficiently than MD. We must stress that Figure 2 depicts the three-dimensional diffusion coefficient, while Figure 3 depicts specifically the diffusivity along the [010] direction. Therefore, they are not necessarily equal. In particular, transport along the [100] axis is slightly more favored when using RSM-GSHMC, and this is reflected in Figure 3.

The noise in the MSD curves in Figure 3 is at least partially due to the fact that a fraction of the $Na^+$ atoms do not perform any jump or jump only once, as illustrated in Figure 6a. While the situation could be improved by extending the simulations, the fact, that the polarizable core–shell model involves a very light particle (the shell), severely limits the simulation time-step, and further increasing the simulation time comes with a significant increase in the computation time.
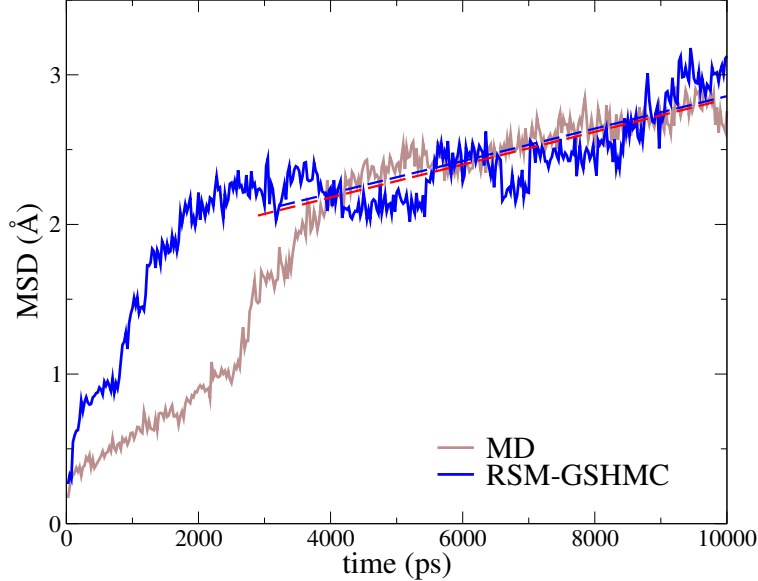
Figure 3: MSD at 700 K in the main diffusion direction, [010], using both traditional MD and RSM-GSHMC combined with $Na_xFePO_4$-ff. Convergence to the equilibrium slope is reached faster through RSM-GSHMC.

# Results and Discussion

## Study of Diffusion of $Na^+$ in $Na_{0.66}FePO_4$

Since $Na^+$ diffusion is an activated process with an energy barrier of 0.32–0.44 eV,[30,34,35] its study cannot be easily accessed through classical MD methods. Moreover, the absence of suitable force fields for $x < 1$ has constrained previous studies to fully sodiated $NaFePO_4$ by creating few $Na^+$ vacancies in the lattice.[30] First-principles analysis of diffusion in $Na_{0.93}FePO_4$ have determined that $Na^+$ transport is limited to the [010] direction, on a curved path that is perpendicular to the faces below the shared edges of $NaO_6$ tehtrahedra (Figure 4). The estimated activation energies range from 0.38 to 0.44 eV.[34,35] A lower activation energy of 0.32 eV was obtained by Tripathi et al.[30] using the Mott-Littleton scheme incorporated in the GULP code[73] and Whiteside-ff.

We use the RSM-GSHMC hybrid Monte Carlo scheme[29,67,68,74] to explore for the first time diffusion of $Na^+$ in $Na_{0.66}FePO_4$, a relevant intermediate phase during the intercalation/deintercalation process. The previous study using Whiteside-ff has demonstrated the

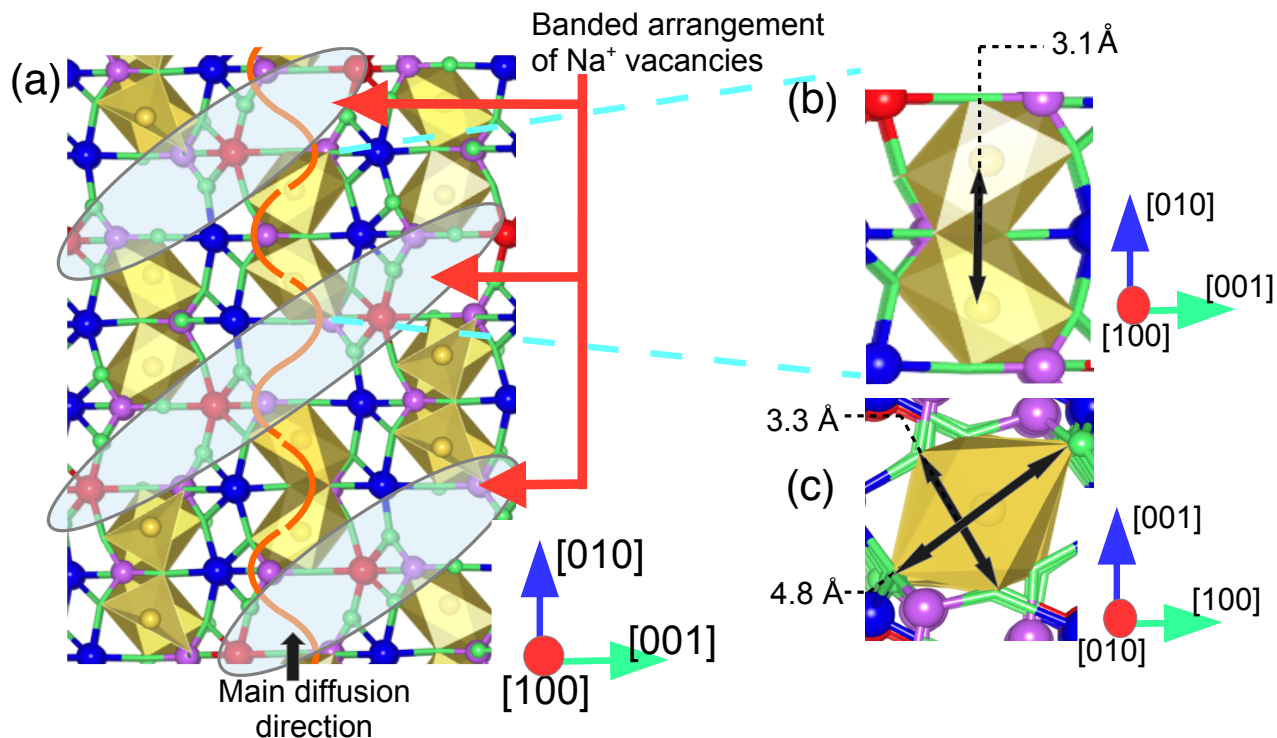Figure 4: (a) Structure of olivine $Na_{0.66}FePO_4$. The octahedral coordination around $Na^+$ are shown in yellow, while the remaining atomic species are color coded as follows: $O^{2+}$ in green, $P^{5+}$ in purple, $Fe^{2+}$ in blue and $Fe^{3+}$ in red. The curved trajectory followed by $Na^+$[31,35] along one of the channels in the main diffusion direction, [010], is depicted as the solid orange line. $Na^+$ vacancies and $Fe^{3+}$ ions follow the banded arrangement displayed in the figure. (b) Linear distance between $Na^+$ sites in the [010] direction is 3.1 Å. This is the length of individual $Na^+$ jumps. (c) Cross section of a diffusion channel along [010]. The dimensions of the channel are measured between oxygen centers. The channels along [001] are much narrower, suggesting that jumps in this direction would be rare in defect free structures. The [100] is fully blocked.

ability of RSM-GSHMC to improve sampling over traditional MD in $NaFePO_4$.[29] Hence, the method's efficiency has been validated for this type of systems and the relatively small changes in the force field proposed here are not expected to deteriorate it.

Using classical MD, Boulfelfel et al.[75] showed that, at 1200 K, it takes an average of 1200 ps to generate a single Frenkel defect in $LiFePO_4$. A similar time scale is reasonably expected to operate for $NaFePO_4$: while $Na^+$ ions are larger than Li ions, the channel cross section in $NaFePO_4$ is larger than that in $LiFePO_4$, somewhat compensating the ion size effect.[30] Consequently, long 10 ns simulations were performed at 300 K, 500 K, and 700 K.
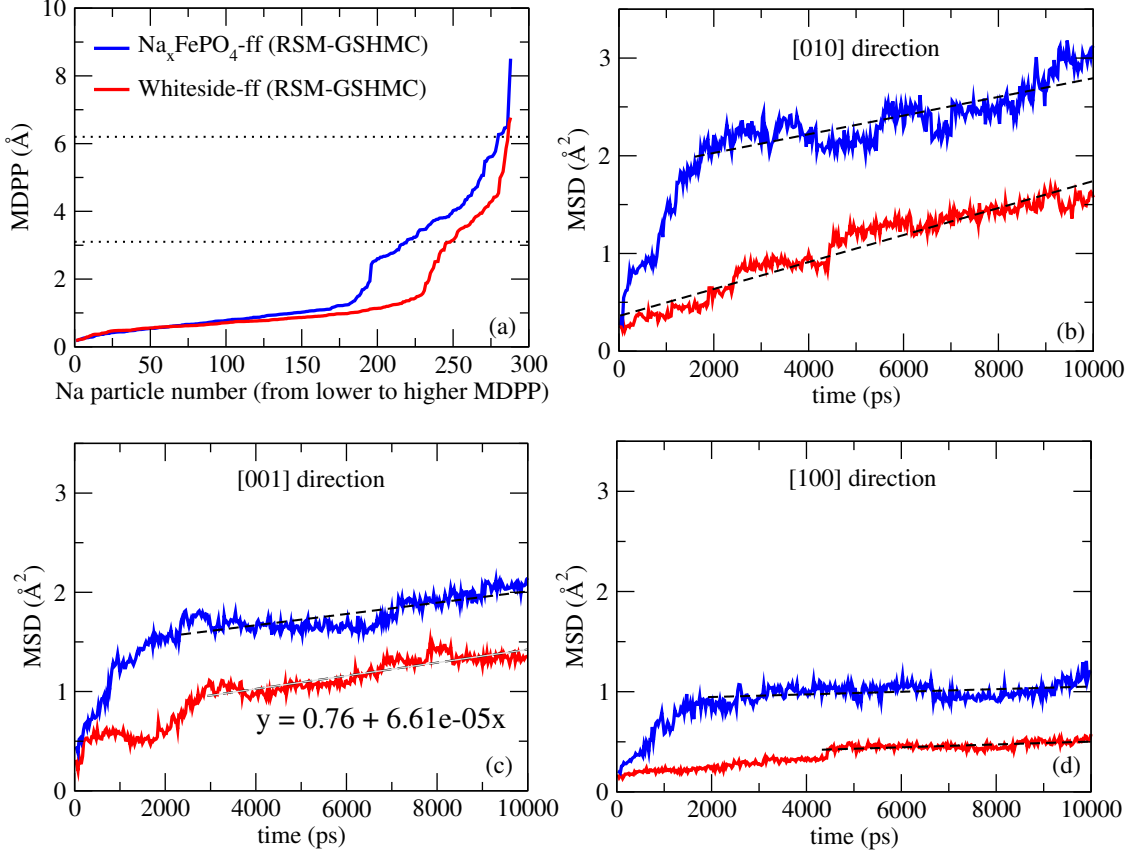
Figure 5: 10 ns simulation of $Na_{0.66}FePO_4$ at 700 K in the NPT ensamble using RSM-GSHMC with $Na_xFePO_4$-ff (blue) and Whiteside et al.-ff (red). (a) MDPP during the 10 ns run. The particles are ordered from minimum to maximum displacement. The dashed lines represent displacements that must involve jumps between $Na^+$ sites. (b), (c), and (d) show the MSD vs time along the [010], [001], and [100] directions, respectively.

Figure 5(a) depicts the maximum displacement per particle (MDPP) during a 10 ns run using RSM-GSHMC with $Na_xFePO_4$-ff and Whiteside-ff. The dashed horizontal lines represents displacements a particle must perform in order to jump to an adjacent cavity. Notably, in comparison to Whiteside-ff, $Na_xFePO_4$-ff allows for a larger proportion of particles ($\sim 20\%$) to jump between cavities over the simulation time, thus producing a higher diffusion coefficient (Figures 5(b) - (c)). This does not necessarily mean that Whiteside-ff produces less accurate diffusivity results. However, the underestimated volumetric expansion of the structure, observed in Figure 1 at 700 K with Whiteside-ff, may, indeed, lead to slightly narrower channels and more constrained displacements and, as a result, to the

underestimated diffusivity.

Figure 6(a) shows the MDPP after a 10 ns RSM-GSHMC run with $Na_xFePO_4$-ff at 300 and 500 K. As expected, the number of hopping particles is significantly lower compared to that at 700 K (see Figure 5). Nevertheless, the MSD in the [010] direction presented in Figure 6(b) is monotonically linear and provides a measure of the diffusion coefficient. Interestingly, the slope of the MSD curve in the [001] direction is considerably lower than that at 700 K, suggesting that a higher temperature promotes transport through the narrower paths perpendicular to the main diffusion axis. This behavior was also captured in MD simulations of $LiFePO_4$ at 500 K,[75] occurring at a rate of 1 or 2 events every 60 ps. In our case, this is potentially a consequence of the volumetric expansion of the structure together with thermally induced disorder. As a matter of fact, the heat treatment is known to transform olivine $NaFePO_4$ into the more thermodynamically stable maricite phase.[76]
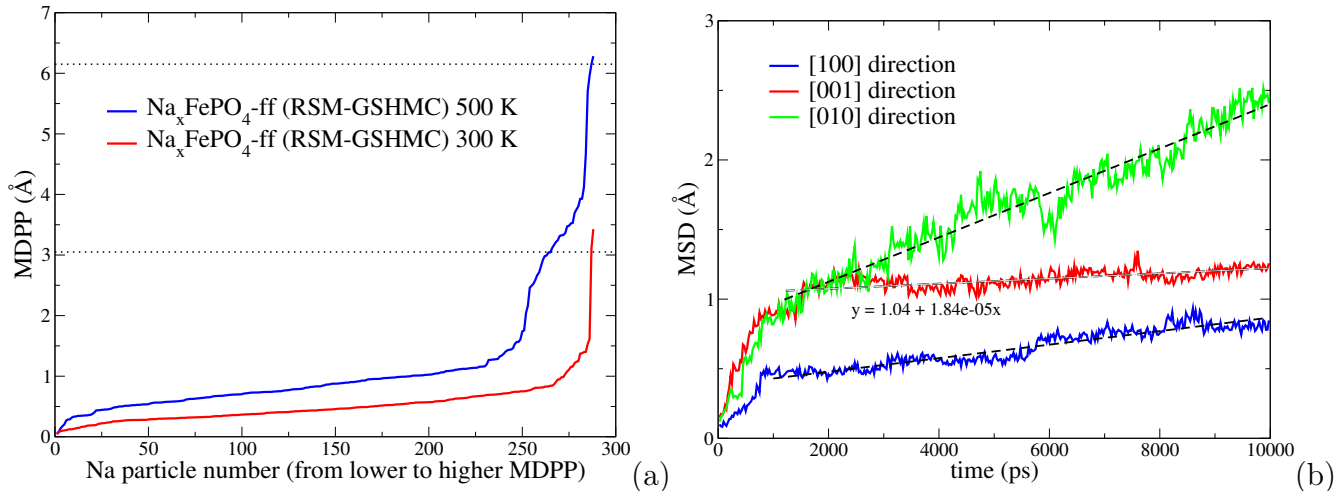


Figure 6: (a) MDPP after a 10 ns run at 300 and 500 K. (b) MSD vs time along the [010], [100], and [001] directions for 10 ns simulation at 500 K.

At 300 K, diffusion is severely limited. Galvanostatic measurements estimate a diffusion coefficient of $10^{-17}$ cm$^2$/s,[21] substantially below what can be probed through MD simulations. While this macroscopic result likely incorporates a number of additional resistances, it is evident that considerably larger simulation times are required to obtain an accurate estimate.

## MD Trajectories Analysis at 700 K

During an MD run, it is important to distinguish between two types of vacancies in the structure of olivine $Na_xFePO_4$. On the one hand, there are *extrinsic vacancies* associated with the absence of $Na^+$ with respect to the stoichiometric structure. These vacancies are located in bands along the [011] direction and separated by $Fe^{3+}O_6$ octahedra, as shown in Figure 4. On the other hand, there are *intrinsic vacancies* associated with the formation of Frenkel defects during $Na^+$ diffusion.

Figure 7 displays an interesting trajectory observed at 700 K. It also presents the typical passage of $Na^+$ through the extrinsic vacancies, not previously observed in MD studies. In the past, Tealdi et al.[77] simulated diffusion in $Li_{0.75}FePO_4$ using classical MD by assigning a formal charge of $+2.25$ to all Fe ions. Because of the uniformity in the Fe charges, the initial Li vacancies were distributed randomly, and their positions could vary freely over the course of the simulations. Our approach is fundamentally different as it distinguishes between $Fe^{2+}$ and $Fe^{3+}$, putting stringent constraints on the possible location of the extrinsic vacancies (see Figure 4). Over the course of our simulations extrinsic vacancies remain fixed, perturbed only by the temporary presence of $Na^+$ and $Fe^{2+}$ ions. Hence, Tealdi et al. study represents the limit of very fast polaron diffusion, while our study is concerned with the limit of very slow (with respect to $Na^+$ mobility) polaron diffusion.

The presence of four diametrically opposed $Fe^{3+}$ ions around extrinsic vacancies, as indicated by the double arrow in Figure 7(a), makes this type of vacancies highly repulsive to $Na^+$. Even under these circumstances, formation of an intrinsic vacancy due to diffusion of the pink $Na^+$ (jump 3 in Figure 7(b)) immediately prompts the rapid transport of the cyan-labeled particle through the extrinsic vacancy, following the S-shaped trajectory presented in jump 4 of Figure 7(b). Similarly, diffusion of the cyan $Na^+$ to the adjacent site, as depicted in jump 8 of Figure 7(c), activates the rapid transport of the orange ion trough the extrinsic vacancy, following the S-shaped trajectory shown in jump 9 of Figure 7(c). In both cases, the residence time of $Na^+$ in the extrinsic vacancy site is below 2 ps, which means that the

entire movement, $\sim 6.2$ Å in length, can essentially be considered as a single long jump.

Na$^+$/Fe$^2$+ "antisite" pair defects occur when one Na$^+$ (ionic radius 1.02 Å) and one Fe$^{2+}$ (ionic radius 0.78 Å) are interchanged between their two nonequivalent M1 and M2 octahedral sites. For olivine LiFePO$_4$, the prevalence of Li$^+$/Fe$^{2+}$ antisite defects is $\sim$1-2% at room temperature.[32,33,78,79] Since there is a considerable difference in radius between Na$^+$/Fe$^{2+}$ compared to Li$^+$/Fe$^2$+ (ionic radius 0.74 Å for Li$^+$), it is expected for Na$^+$/Fe$^{2+}$ antisites to be far less frequent. However, classical atomistic simulations indicate that the Na$^+$/Fe$^{2+}$ antisite formation energy (0.86 eV) is comparable to that of Li$^+$/Fe$^{2+}$ antisite (0.74 eV).[30] Hence, the prevalence of Na$^+$/Fe$^{2+}$ antisites in NaFePO$_4$ is also likely to be $\sim$1-2%. Notice that the presence of these defects blocks Na$^+$ diffusion along the [010] direction.

Let us refer again to LiFePO$_4$. For this cathode, computational and experimental studies have shown that nanosize particles (100 nm) would be delithiated in less than 0.01 s, given that the [010] chanels are nearly defect free. Even with only one defect per channel, there would still be accessible charge carriers from the particle surface. In contrast, conductivity studies performed by Amin et al.[80] on macroscopic (millimeter scale) LiFePO$_4$ single crystals produce much lower diffusivities and more isotropic transport (i.e., diffusion perpendicular to the [010] channel becomes more likely). DFT studies covering an exhaustive number of diffusion paths[81] produced 2D diffusivities (along the [010] and [001] directions: $y$ and $z$ axes in Figure 7) that approximate better those experimentally observed in macrosocpic LiFePO$_4$ than DFT-based diffusivities along [010] only .

While the effect of anisotropic diffusion in NaFePO$_4$ has not been as extensively studied, the large discrepancies between the theoretically estimated one-dimensional diffusion coefficient ($\sim 10^{-10}$ cm$^2$/s[35]) and that obtained from macroscopic measurements ($\sim 10^{-17}$ cm$^2$/s[21]) indicate that, on large scale devices, it could be quite significant. Our simulations show, for the first time, that the blockage of the main diffusion channel ([010] direction) by Fe$^{2+}$ can in fact estimulate mobility in the [001] direction, potentially reducing the overall two-dimensional diffusivity but allowing sodiation/desodiation to continue despite the tem-

porary or permanent $Fe^{2+}$ blockage of a diffusion channel. Figure 7 illustrates the mechanics of this process. A $Fe^{2+}$ ion can temporarily occupy an extrinsic vacancy (jump 1, Figure 7(b)), leading to the formation of an antisite - like defect when the nearest $Na^+$ ion (green particle) moves to the free $Fe^{2+}$ site (jump 2 in Figure 7(b)). Given the difference in size between $Na^+$ and $Fe^{2+}$, it is likely that the local structural deformation permits the transfer of the green $Na^+$ to the adjacent channel (jump 6 in Figure 7(c)) while simultaneously allowing the blocking $Fe^{2+}$ to remain for several tens of ps in the highly repulsive extrinsic vacancy. A second sodium transfers to the adjacent channel (pink particle, jump 12 in Figure 7(d)) before the $Fe^{2+}$ is reabsorbed into its original site (jump 13 in Figure 7(d)). Upon reabsortion, diffusion continues in the preferential direction.

This result is in general agreement with simulations of two-dimensional diffusion in $LiFePO_4$:[75,77,81] occasional jumps of charge carriers in the [001] can overcome (at a cost of reduced diffusivity) the damaging effect of antisite defects. Notably, we did not observe this phenomenon at 300 K. Nonetheless, this could be the result of insufficient simulation times. All other diffusion events follow the trajectories extensively described in the literature.[30,34,75] We believe that increasing simulation times along with the novel simulation techniques such as RSM-GSHMC coupled with $Na_xFePO_4$-ff for the analysis of rare events will allow unveiling the interesting and yet vastly understudied phenomenon of the filling of extrinsic vacancies during actual intercalation/deintercalation processes.
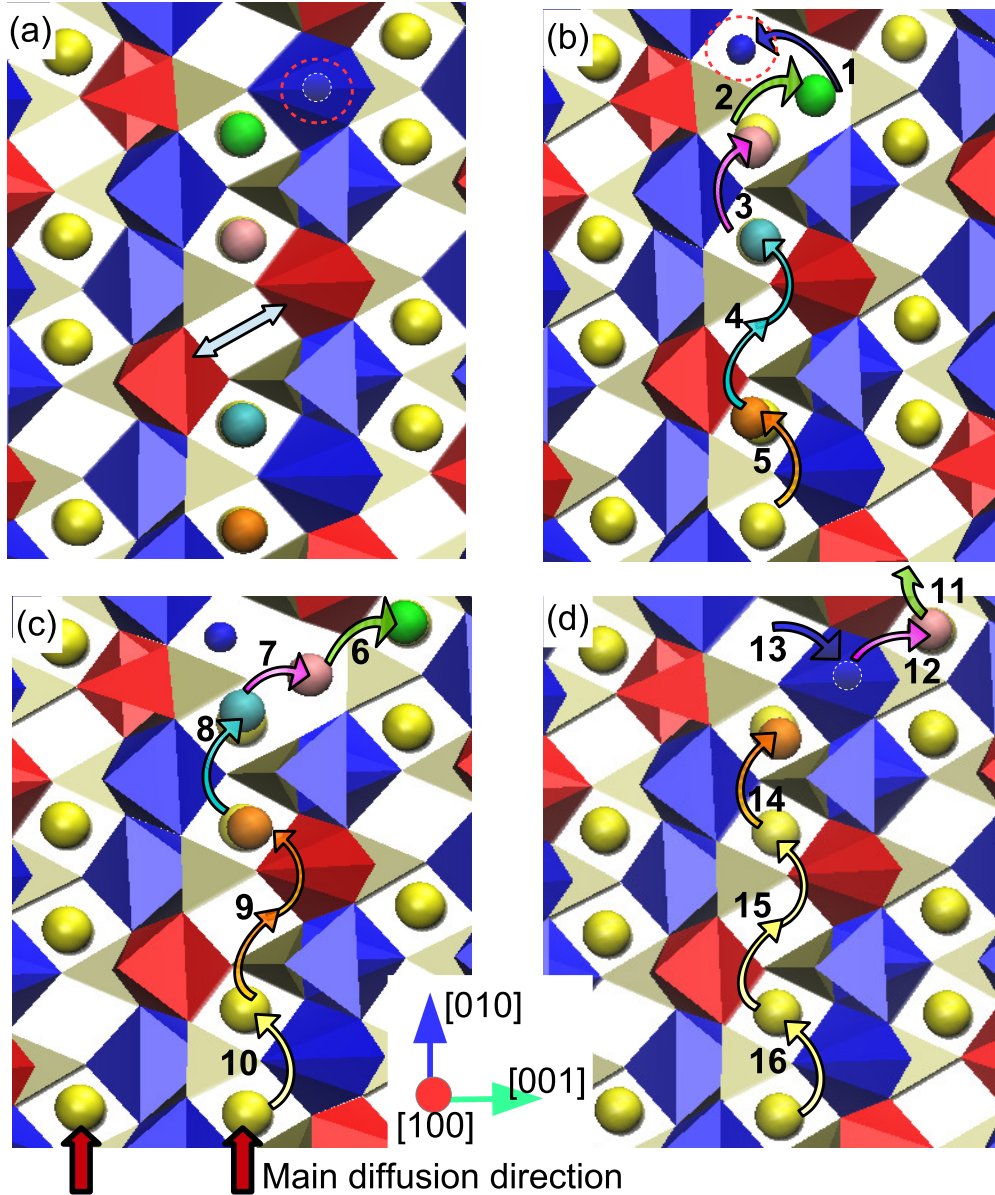
Figure 7: Two-dimensional trajectory at 700 K. At this temperature, the coordination polyhedra are slightly distorted. The red octahedra are $Fe^{3+}O_6$ units, the blue octahedra are $Fe^{2+}O_6$ units, and the tetrahedrals correspond to $(PO_4)^{-3}$ units. The green, pink, cyan and orange atoms are tagged $Na^+$ ions; the remaining $Na^+$ ions are colored in yellow. The numbers in the figure specify the order in which atomic jumps occurred. (a) Initial, defect-free configuration. The double arrow shows the diametrically opposed $Fe^{3+}$ ions around an extrinsic vacancy. (b) Antisite-like defect. A $Fe^{2+}$ atom (encircled in red in (a) and (b)) moves to the adjacent extrinsic vacancy (jump 1), allowing the green $Na^+$ to jump to the empty $Fe^{2+}$ site (jump 2). (c) Since the central diffusion channel is blocked, the green $Na^+$ transfers to an adjacent channel (jump 6), leading to the cascade of jumps 7 – 10. (d) Pink and green $Na^+$ continue diffusing through the adjacent channel. After the defect in the $Fe^{2+}$ site is removed (jump 13), one-dimensional diffusion is restablished. Notice that $Na^+$ diffuses through the extrinsic vacancies in single, long curvilinear jumps (4, 9, and 15).

24

# Conclusions

In this work we developed and validated a polarizable force field for olivine $Na_xFePO_4$. The new force field outperforms existing alternatives in terms of thermal stability, accuracy, and applicability to the whole range of sodium compositions ($0 < x < 1$). In addition, we applied an enhanced sampling methodology based on a shadow hybrid Monte Carlo technique, RSM-GSHMC,[29] in order to access the dynamics of rare events using shorter simulations and lower temperatures than those typically required by atomistic simulations on similar systems. The combination of the new force field and the RSM-GSHMC approach allowed us to study with unprecedented detail Na-ion diffusion in $Na_{0.66}FePO_4$ at the molecular-level. We confirmed that the main diffusion mechanism involves single Na-ion hops through the one-dimensional channels along the [010] crystallographic direction. Furthermore, we identified the novel Na-ion diffusion dynamics involving the formation and annihiliation of $Na^+/Fe^{2+}$ antisite defects, which effectively facilitate the migration of Na-ions between adjacent [010] channels. $Na^+/Fe^{2+}$ antisite defects were expected to block [010] channels and, therefore, hinder Na-ion mobility in the bulk material. In contrast, our results revealed that such defects can indeed favor Na-ion exchange between parallel [010] channels. In principle, similar ion migration mechanisms could operate in other olivine framework compounds as well. Overall, this study provides an in-depth understanding of Na-ion mobility in olivine $Na_xFePO_4$, a promising alternative to the commercially available $LiFePO_4$ cathode material for Na-ion batteries, and paves the way to unveil fundamental aspects of ion dynamics in polyanionic materials, in general.

# Acknowledgement

## Supporting Information Available

Tuning parameters for the simulated annealing algorithm incorporated in *potfit*, as well as the fitting errors are listed in section S1. A new methodology for selecting the position of the shells in the core–shell model is described in section S3. A comparison between $g_{P-P}(r)$ in the $Na_{0.58}FePO_4$ system obtained with Whiteside-ff and $Na_xFePO_4$-ff is shown in section S3. Finally, the relative error in cell volumes obtained with Whiteside-ff and $Na_xFePO_4$-ff is shown in section S4.

## References

(1) Tarascon, J. M. Is lithium the new gold? *Nature Chemistry* **2010**, *2*.

(2) Slater, M. D.; Kim, D.; Lee, E.; Johnson, C. S. Sodium-Ion Batteries. *Advanced Functional Materials* **2013**, *23*, 947–958.

(3) Kundu, D.; Talaie, E.; Duffort, V.; Nazar, L. F. The Emerging Chemistry of Sodium Ion Batteries for Electrochemical Energy Storage. *Angewandte Chemie International Edition* **2015**, *54*, 3431–3448.

(4) Palomares, V.; Serras, P.; Villaluenga, I.; Hueso, K. B.; Carretero-Gonzalez, J.; Rojo, T. Na-ion batteries, recent advances and present challenges to become low cost energy storage systems. *Energy Environ. Sci.* **2012**, *5*, 5884–5901.

(5) Kim, S.-W.; Seo, D.-H.; Ma, X.; Ceder, G.; Kang, K. Electrode Materials for Rechargeable Sodium-Ion Batteries: Potential Alternatives to Current Lithium-Ion Batteries. *Advanced Energy Materials* **2012**, *2*, 710–721.

(6) Hueso, K. B.; Armand, M.; Rojo, T. High temperature sodium batteries: status, challenges and future trends. *Energy Environ. Sci.* **2013**, *6*, 734–749.

(7) Yabuuchi, N.; Kubota, K.; Dahbi, M.; Komaba, S. Research Development on Sodium-Ion Batteries. *Chem. Rev.* **2014**, *114*, 11636–11682.

(8) Pan, H.; Hu, Y.-S.; Chen, L. Room-temperature stationary sodium-ion batteries for large-scale electric energy storage. *Energy Environ. Sci.* **2013**, *6*, 2338–2360.

(9) Han, M. H.; Gonzalo, E.; Singh, G.; Rojo, T. A comprehensive review of sodium layered oxides: powerful cathodes for Na-ion batteries. *Energy Environ. Sci.* **2015**, *8*, 81–102.

(10) Landa-Medrano, I.; Li, C.; Ortiz-Vitoriano, N.; Ruiz de Larramendi, I.; Carrasco, J.; Rojo, T. Sodium–Oxygen Battery: Steps Toward Reality. *The Journal of Physical Chemistry Letters* **2016**, *7*, 1161–1166.

(11) Luo, W.; Shen, F.; Bommier, C.; Zhu, H.; Ji, X.; Hu, L. Na-Ion Battery Anodes: Materials and Electrochemistry. *Accounts of Chemical Research* **2016**, *49*, 231–240.

(12) Kim, H.; Kim, H.; Ding, Z.; Lee, M. H.; Lim, K.; Yoon, G.; Kang, K. Recent Progress in Electrode Materials for Sodium-Ion Batteries. *Advanced Energy Materials* **2016**, *6*, 1600943.

(13) Nitta, N.; Wu, F.; Lee, J. T.; Yushin, G. Li-ion battery materials: present and future. *Materials Today* **2015**, *18*, 252 – 264.

(14) Yazami, R.; Touzain, P. A reversible graphite-lithium negative electrode for electrochemical generators. *Journal of Power Sources* **1983**, *9*, 365–371.

(15) Winter, M.; Besenhard, J. O.; Spahr, M. E.; Novák, P. Insertion Electrode Materials for Rechargeable Lithium Batteries. *Advanced Materials* **1998**, *10*, 725–763.

(16) Ge, P.; Fouletier, M. Electrochemical intercalation of sodium in graphite. *Solid State Ionics* **1988**, *28*, 1172 – 1175.

(17) Jache, B.; Adelhelm, P. Use of Graphite as a Highly Reversible Electrode with Superior Cycle Life for Sodium-Ion Batteries by Making Use of Co-Intercalation Phenomena. *Angewandte Chemie International Edition* **2014**, *53*, 10169–10173.

(18) Moriwake, H.; Kuwabara, A.; Fisher, C. A. J.; Ikuhara, Y. Why is sodium-intercalated graphite unstable? *RSC Adv.* **2017**, *7*, 36550–36554.

(19) Wang, J.; Sun, X. Olivine LiFePO$_4$: the remaining challenges for future energy storage. *Energy Environ. Sci.* **2015**, *8*, 1110–1138.

(20) Fang, Y.; Zhang, J.; Xiao, L.; Ai, X.; Cao, Y.; Yang, H. Phosphate Framework Electrode Materials for Sodium Ion Batteries. *Advanced Science* **2017**, *4*, 1600392.

(21) Zhu, Y.; Xu, Y.; Liu, Y.; Luo, C.; Wang, C. Comparison of electrochemical performances of olivine NaFePO$_4$ in sodium-ion batteries and olivine LiFePO$_4$ in lithium-ion batteries. *Nanoscale* **2013**, *5*, 780–787.

(22) Galceran, M.; Roddatis, V.; Zúñiga, F. J.; Pérez-Mato, J. M.; Acebedo, B.; Arenal, R.; Peral, I.; Rojo, T.; Casas-Cabanas, M. Na-Vacancy and Charge Ordering in Na$_{\approx 2/3}$FePO$_4$. *Chem. Mater.* **2014**, *26*, 3289–3294.

(23) Galceran, M.; Saurel, D.; Acebedo, B.; Roddatis, V. V.; Martin, E.; Rojo, T.; Casas-Cabanas, M. The mechanism of NaFePO4 (de)sodiation determined by in situ X-ray diffraction. *Phys. Chem. Chem. Phys.* **2014**, *16*, 8837–8842.

(24) Boucher, F.; Gaubicher, J.; Cuisinier, M.; Guyomard, D.; Moreau, P. Elucidation of the

Na$_{2/3}$FePO$_4$ and Li$_{2/3}$FePO$_4$ Intermediate Superstructure Revealing a Pseudouniform Ordering in 2D. *Journal of the American Chemical Society* **2014**, *136*, 9144–9157.

(25) Casas-Cabanas, M.; Roddatis, V. V.; Saurel, D.; Kubiak, P.; Carretero-Gonzalez, J.; Palomares, V.; Serras, P.; Rojo, T. Crystal chemistry of Na insertion/deinsertion in FePO4-NaFePO4. *J. Mater. Chem.* **2012**, *22*, 17421–17423.

(26) Malik, R.; Zhou, F.; Ceder, G. Kinetics of non-equilibrium lithium incorporation in LiFePO$_4$. *Nature materials* **2011**, *10 8*, 587–590.

(27) Hess, M.; Sasaki, T.; Villevieille, C.; Novák, P. Combined *operando* X-ray diffraction–electrochemical impedance spectroscopy detecting solid solution reactions of LiFePO$_4$ in batteries. *Nature communications* **2015**, *6*, 8169.

(28) Liu, H.; Strobridge, F. C.; Borkiewicz, O. J.; Wiaderek, K. M.; Chapman, K. W.; Chupas, P. J.; Grey, C. P. Capturing metastable structures during high-rate cycling of LiFePO$_4$ nanoparticle electrodes. *Science* **2014**, *344*.

(29) Escribano, B.; Lozano, A.; Radivojević, T.; Fernández-Pendás, M.; Carrasco, J.; Akhmatskaya, E. Enhancing sampling in atomistic simulations of solid-state materials for batteries: a focus on olivine NaFePO$_4$. *Theoretical Chemistry Accounts* **2017**, *136*, 43.

(30) Tripathi, R.; Wood, S. M.; Islam, M. S.; Nazar, L. F. Na-ion mobility in layered Na$_2$FePO$_4$F and olivine Na[Fe,Mn]PO$_4$. *Energy and Environmental Science* **2013**, *6*, 2257–2264.

(31) Whiteside, A.; Fisher, C.; Parker, S.; Islam, M. S. Particel shapes and surface structures of olivine NaFePO$_4$ in comparison to LiFePO$_4$. *Phys. Chem. Chem. Phys.* **2014**, *16*, 21788–21794.

(32) Islam, M.; Driscoll, D.; Fisher, C.; Slater, P. Atomic-scale investigation of defects, dopants, and lithium transport in the $LiFePO_4$ olivine-type battery material. *Chem. Mater.* **2005**, *17*, 5085–5092.

(33) Chung, S.-Y.; Choi, S.-Y.; Yamamoto, T.; Ikuhara, Y. Atomic-Scale Visualization of Antisite Defects in $LiFePO_4$. *Phys. Rev. Lett.* **2008**, *100*, 125502.

(34) Ong, S. P.; Chevrier, V. L.; Hautier, G.; Jain, A.; Moore, C.; Kim, S.; Ma, X.; Ceder, G. Voltage, stability and diffusion barrier differences between sodium-ion and lithium-ion intercalation materials. *Energy Environ. Sci.* **2011**, *4*, 3680–3688.

(35) Dixit, M.; Engel, H.; Eitan, R.; Aurbach, D.; Levi, M. D.; Kosa, M.; Major, D. T. Classical and Quantum Modeling of Li and Na Diffusion in $FePO_4$. *The Journal of Physical Chemistry C* **2015**, *119*, 15801–15809.

(36) Pedone, A.; Malavasi, G.; Menziani, M. C.; Cormack, A. N.; Segre, U. A New Self-Consistent Empirical Interatomic Potential Model for Oxides, Silicates, and Silica-Based Glasses. *The Journal of Physical Chemistry B* **2006**, *110*, 11780–11795, PMID: 16800478.

(37) Ong, S. P.; Andreussi, O.; Wu, Y.; Marzari, N.; Ceder, G. Electrochemical Windows of Room-Temperature Ionic Liquids from Molecular Dynamics and Density Functional Theory Calculations. *Chemistry of Materials* **2011**, *23*, 2979–2986.

(38) Burbano, M.; Carlier, D.; Boucher, F.; Morgan, B. J.; Salanne, M. Sparse Cyclic Excitations Explain the Low Ionic Conductivity of Stoichiometric $Li_7La_3Zr_2O_{12}$. *Phys. Rev. Lett.* **2016**, *116*, 135901.

(39) Galvez-Aranda, D. E.; Ponce, V.; Seminario, J. M. Molecular dynamics simulations of the first charge of a Li-ion—Si-anode nanobattery. *Journal of Molecular Modeling* **2017**, *23*, 120.

(40) Mitchell, P.; Fincham, D. Shell model simulations by adiabatic dynamics. *J. Phys.: Condens. Matter* **1993**, *5*, 1031.

(41) Yan, T.; Burnham, C. J.; Del Pópolo, M. G.; Voth, G. A. Molecular Dynamics Simulation of Ionic Liquids: The Effect of Electronic Polarizability. *The Journal of Physical Chemistry B* **2004**, *108*, 11877–11881.

(42) Beck, P.; Brommer, P.; Roth, J.; Trebin, H.-R. Ab initio based polarizable force field generation and application to liquid silica and magnesia. *The Journal of Chemical Physics* **2011**, *135*, 234512.

(43) Beck, P.; Brommer, P.; Roth, J.; Trebin, H.-R. Influence of polarizability on metal oxide properties studied by molecular dynamics simulations. *Journal of Physics: Condensed Matter* **2012**, *24*, 485401.

(44) Dick, B. G.; Overhauser, A. W. Theory of the Dielectric Constants of Alkali Halide Crystals. *Phys. Rev.* **1958**, *112*, 90 – 103.

(45) Fumi, F.; Tosi, M. Ionic sizes and born repulsive parameters in the NaCl-type alkali halides—I. *Journal of Physics and Chemistry of Solids* **1964**, *25*, 31 – 43.

(46) Lindan, P.; Gillan, M. Shell-model molecular dynamics simulation of superionic conduction in $CaF_2$. *J. Phys.: Condens. Matter* **1993**, *5*, 1019.

(47) Brommer, P.; Gähler, F. Potfit: effective potentials from ab initio data. *Modelling and Simulation in Materials Science and Engineering* **2007**, *15*, 295.

(48) Brommer, P.; Kiselev, A.; Schopf, D.; Beck, P.; Roth, J.; Trebin, H.-R. Classical interaction potentials for diverse materials from ab initio data: a review of potfit. *Modelling and Simulation in Materials Science and Engineering* **2015**, *23*, 074002.

(49) Ercolessi, F.; Adams, J. B. Interatomic Potentials from First-Principles Calculations: The Force-Matching Method. *EPL (Europhysics Letters)* **1994**, *26*, 583.

(50) Kresse, G.; Furthmuller, J. Efficiency of ab-initio total energy calculations for metals and semiconductors using a plane-wave basis set. *Comput. Mat. Sci.* **1996**, *6*, 15.

(51) Kresse, G.; Hafner, J. Ab initio molecular dynamics for liquid metals. *Phys. Rev. B* **1993**, *47*, 558.

(52) Kresse, G.; Hafner, J. Ab initio molecular-dynamics simulation of the liquid-metal-amorphous-semiconductor transition in germanium. *Phys. Rev. B* **1994**, *49*, 14251.

(53) Saracibar, A.; Carrasco, J.; Saurel, D.; Galceran, M.; Acebedo, B.; Anne, H.; Lepoitevin, M.; Rojo, T.; Casas Cabanas, M. Investigation of sodium insertion-extraction in olivine $Na_x FePO_4$ ($0 \leq x \leq 1$) using first-principles calculations. *Phys. Chem. Chem. Phys.* **2016**, *18*, 13045–13051.

(54) Perdew, J. P.; Burke, K.; Ernzerhof, M. Generalized Gradient Approximation Made Simple. *Phys. Rev. Lett.* **1996**, *77*, 3865–3868.

(55) Dudarev, S. L.; Botton, G. A.; Savrasov, S. Y.; Szotek, Z.; Temmerman, W. M.; Sutton, A. P. Electronic Structure and Elastic Properties of Strongly Correlated Metal Oxides from First Principles: LSDA + U, SIC-LSDA and EELS Study of UO2 and NiO. *physica status solidi (a)* **1998**, *166*, 429–443.

(56) Zhou, F.; Cococcioni, M.; Marianetti, C. A.; Morgan, D.; Ceder, G. First-principles prediction of redox potentials in transition-metal compounds with LDA+*U*. *Phys. Rev. B* **2004**, *70*, 235121.

(57) Nosé, S. A unified formulation of the constant temperature molecular dynamics methods. *The Journal of Chemical Physics* **1984**, *81*, 511–519.

(58) Hess, B.; Kutzner, C.; van der Spoel, D.; Lindahl, E. Gromacs 4: Algorithms for highly efficient, load-balanced, and scalable molecular simulation. *J. Chem. Theory Comput.* **2008**, *4*, 435–447.

(59) Duane, S.; Kennedy, A. D.; Pendleton, B. J.; Roweth, D. Hybrid Monte Carlo. *Physics Letters B* **1987**, *195*, 216–222.

(60) Horowitz, A. M. A generalized guided Monte Carlo algorithm. *Physics Letters B* **1991**, *268*, 247 – 252.

(61) Akhmatskaya, E.; Reich, S. GSHMC: An efficient method for molecular simulation. *Journal of Computational Physics* **2008**, *227*, 4934 – 4954.

(62) Blanes, S.; Casas, F.; Sanz-Serna, J. M. Numerical integrators for the Hybrid Monte Carlo method. *SIAM Journal on Scientific Computing* **2014**, *36 (4)*, A1556 – A1580.

(63) Fernández-Pendás, M.; Akhmatskaya, E.; Sanz Serna, J. Adaptive multi-stage integrators for optimal energy conservation in molecular simulations. *Journal of Computational Physics* **2016**, *327*, 434 – 449.

(64) Akhmatskaya, E.; Fernández-Pendás, M.; Radivojević, T.; Sanz-Serna, J. M. Adaptive Splitting Integrators for Enhancing Sampling Efficiency of Modified Hamiltonian Monte Carlo Methods in Molecular Simulation. *Langmuir* **2017**, *0*, null, DOI: 10.1021/acs.langmuir.7b01372.

(65) Escribano, B.; Akhmatskaya, E.; Mujika, J. Combining stochastic and deterministic approaches within high efficiency molecular simulations. *Central European Journal of Mathematics* **2013**, *11*, 787–799.

(66) Fernández-Pendás, M.; Escribano, B.; Radivojević, T.; Akhmatskaya, E. Constant pressure hybrid Monte Carlo simulations in GROMACS. *Journal of Molecular Modeling* **2014**, *20*.

(67) Akhmatskaya, E.; Reich, S. Meso-GSHMC: A stochastic algorithm for meso-scale constant temperature simulations. *Procedia Computer Science* **2011**, *4*, 1353 – 1362.

(68) Escribano, B.; Akhmatskaya, E.; Reich, S.; Azpiroz, J. Multiple-time-stepping generalized hybrid Monte Carlo methods. *Journal of Computational Physics* **2015**, *280*, 1—20.

(69) Wee, C.; Samson, M.; Reich, S.; Akhmatskaya, E. Improved sampling for simulations of interfacial membrane proteins: application of generalized shadow hybrid Monte Carlo to a peptide toxin/bilayer system. *J. Phys. Chem. B* **2008**, *112*, 5710 – 5717.

(70) Andersen, H. C. Molecular dynamics simulations at constant pressure and/or temperature. *J. Chem. Phys.* **1980**, *72*, 2384–2393.

(71) Moreau, P.; Guyomard, D.; Gaubicher, J.; Boucher, F. Structure and Stability of Sodium Intercalated Phases in Olivine $FePO_4$. *Chem. Mater.* **2010**, *22*, 4126–4128.

(72) Krishna, R.; van Baten, J. M. A molecular dynamics investigation of the diffusion characteristics of cavity-type zeolites with 8-ring windows. *Microporous and Mesoporous Materials* **2011**, *137*, 83 – 91.

(73) Gale, J. D.; Rohl, A. L. The General Utility Lattice Program (GULP). *Molecular Simulation* **2003**, *29*, 291–341.

(74) Wee, C. L.; Sansom, M. S. P.; Reich, S.; Akhmatskaya, E. Improved Sampling for Simulations of Interfacial Membrane Proteins: Application of Generalized Shadow Hybrid Monte Carlo to a Peptide Toxin/Bilayer System. *The Journal of Physical Chemistry B* **2008**, *112*, 5710–5717.

(75) Boulfelfel, S. E.; Seifert, G.; Leoni, S. Atomistic investigation of Li+ diffusion pathways in the olivine $LiFePO_4$ cathode material. *J. Mater. Chem.* **2011**, *21*, 16365–16372.

(76) Clark, J. M.; Nishimura, S.-i.; Yamada, A.; Islam, M. S. High-Voltage Pyrophosphate Cathode: Insights into Local Structure and Lithium-Diffusion Pathways. *Angewandte Chemie International Edition* **2012**, *51*, 13149–13153.

(77) Tealdi, C.; Spreafico, C.; Mustarelli, P. Lithium diffusion in Li1-xFePO4: the effect of cationic disorder. *J. Mater. Chem.* **2012**, *22*, 24870–24876.

(78) Chung, S.-Y.; Choi, S.-Y.; Yamamoto, T.; Ikuhara, Y. Orientation-Dependent Arrangement of Antisite Defects in Lithium Iron(II) Phosphate Crystals. *Angewandte Chemie International Edition* **2009**, *48*, 543–546.

(79) Islam, M. S.; Fisher, C. A. J. Lithium and sodium battery cathode materials: computational insights into voltage, diffusion and nanostructural properties. *Chem. Soc. Rev.* **2014**, *43*, 185–204.

(80) Amin, R.; Balaya, P.; Maier, J. Anisotropy of Electronic and Ionic Transport in LiFePO4 Single Crystals. *Electrochemical and Solid-State Letters* **2007**, *10*, A13–A16.

(81) Malik, R.; Burch, D.; Bazant, M.; Ceder, G. Particle Size Dependence of the Ionic Diffusivity. *Nano Letters* **2010**, *10*, 4123–4127.